Solar cycle and seasonal variability of H in the upper atmosphere of Mars

Majd Mayyasi, John T. Clarke, Jean-Yves Chaufray, D. Kass, S. Bougher, D. Bhattacharyya, J. Deighan, S. Jain, N. Schneider, G.L. Villanueva, et al.

Icarus 393 (2023) 115293

Contents lists available at ScienceDirect

Icarus

journal homepage: www.elsevier.com/locate/icarus

Solar cycle and seasonal variability of H in the upper atmosphere of Mars

Majd Mayyasi [a,*], John Clarke [b], J.-Y. Chaufray [c], D. Kass [d], S. Bougher [e], D. Bhattacharyya [f], J. Deighan [f], S. Jain [f], N. Schneider [f], G.L. Villanueva [g], F. Montmessin [c], M. Benna [h,i], P. Mahaffy [h], B. Jakosky [f]

[a] Center for Space Physics, Boston University, Boston, MA 02215, United States of America
[b] Astronomy Department, Boston University, Boston, MA 02215, United States of America
[c] Laboratoire Atmosphères, Milieux, Observations Spatiales (LATMOS), UVSQ Université Paris-Saclay, Sorbonne Université, CNRS, Paris, France
[d] Jet Propulsion Laboratory, California Institute of Technology, Pasadena, CA, USA
[e] Climate and Space Sciences and Engineering Department, University of Michigan, Ann Arbor, MI, USA
[f] LASP, University of Colorado Boulder, Boulder, CO, USA
[g] NASA Goddard Space Flight Center, Greenbelt, MD, USA
[h] Solar System Exploration Division, NASA Goddard Space Flight Center, Greenbelt, MD, USA
[i] Center for Space Sciences and Technology, University of Maryland Baltimore County, Baltimore, MD, USA

ARTICLE INFO

Keywords:
Mars
Water loss
H escape
Upper atmosphere

ABSTRACT

The complex seasonal, dust, and atmospheric circulation patterns at Mars affect the abundance and spatial extent of water and its photo-dissociated atomic byproduct H. Recent observations by the Mars Atmosphere and Volatile Evolution (MAVEN) mission have been used to constrain the H abundance at the exobase (200 km altitude) as well as its thermal and global escape rate. The MAVEN observations span the last seven years and encompass the effects of the declining phase of Solar Cycle 24 and activating phase of Solar Cycle 25 from mid-perihelion of Mars Year (MY) 32 through most of aphelion of MY36. Results show that there are seasonal as well as solar cycle variations in H exobase temperatures, densities, thermal escape rates, and global escape rates. During perihelion of MYs 32–35, the H exobase density fluctuates with a cadence that corresponds to the approach to perihelion as well as the onset and peak of regional dust storms. Additionally, the abundance of H atoms did not show exceptional variability during the MY34 Global Dust Storm, when compared with trends from adjacent years. Seasonal averages of H exobase densities, thermal escape rates, and global escape rates indicated an order of magnitude difference between perihelion and aphelion, and suggest a water global equivalent layer range of 0.02–13 m lost over 4 billon years. H properties are also found to vary with solar cycle to a lesser extent than with seasons across the MAVEN timeline. Trends show that the exobase density varies inversely with solar activity, while both the thermal and global escape rates vary directly with solar activity. It remains to be seen if the effects of a stronger than recent solar cycle on the upper atmospheric H properties would become more pronounced.

1. Introduction

Exploration of present-day Mars indicates a wet planet existed in earlier epochs. Theories indicate the planet has since either largely lost its water reservoirs to outer space and/or recirculated much of it into the crust (Villanueva et al., 2015; Orosei et al., 2018; Scheller et al., 2021 and references therein). To understand the mechanics of this escape, the factors that control present-day water loss are being rigorously investigated by multiple surface- and space-based missions (e.g. Zurek et al., 2011; Jakosky et al., 2017). Initial theories of water propagation and loss assumed surface H_2O molecules to propagate to higher altitudes in the form of H_2 where they are dissociated by EUV sunlight into smaller molecules and atoms that can then escape with a total timescale of many tens of years (Hunten, 1982; McElroy and Donahue, 1972; Yung et al., 1988). However, recent observations have shown that atmospheric water vapor varies at much faster timescales (weeks to months), introducing a new paradigm for how water propagates and escapes the planet (Clarke et al., 2014; Clarke, 2018; Chaffin et al., 2014; Chaffin et al., 2017; Chaffin et al., 2021; Heavens et al., 2018; Stone et al., 2020; Patel et al., 2021; Qin, 2021).

* Corresponding author.
E-mail address: majdm@bu.edu (M. Mayyasi).

https://doi.org/10.1016/j.icarus.2022.115293
Received 28 February 2021; Received in revised form 22 April 2022; Accepted 23 September 2022
Available online 30 September 2022

In the lower atmosphere (below 100 km) water retains its molecular form as H_2O vapor (e.g., Fedorova et al., 2006; Alday et al., 2021; Villanueva et al., 2021). Lower atmospheric H_2O abundances have been seen to vary with topography, latitude, seasons (defined by solar longitude, Ls), and ambient dust conditions (e.g., Novak et al., 2011; Villanueva et al., 2015; Villanueva et al., 2022; Aoki et al., 2015; Aoki et al., 2019; Encrenaz et al., 2016; 2018; Fedorova et al., 2017; Fedorova et al., 2020; Belyaev et al., 2021; Jakosky, 2021). H_2O molecules that reach 80–100 km altitudes are photo-dissociate into H atoms by ion-chemical reactions in the upper atmosphere (>100 km) (Shaposhnikov et al., 2022). H atoms above 80 km can diffuse up to higher altitudes where they can escape into space by the evaporative or Jeans process, while the molecules are too heavy to effectively boil off the top of the atmosphere.

A global dust storm in 2018 supplied the upper atmosphere of Mars with enhanced water from lower altitudes, and studies have attributed atmospheric chemistry as a likely driver of the subsequent preferential escape of H (Heavens et al., 2018; Stone et al., 2020). Recent observations have shown that H atoms in the upper atmosphere display variations on timescales that are similar to its parent molecule (H_2O) variability timescales (Clarke et al., 2017; Mayyasi et al., 2017a, 2017b; Mayyasi et al., 2018a; Mayyasi et al., 2019a; Chaffin et al., 2021). The temperatures and abundances of H atoms at the exobase are metrics used to determine their thermal escape and to identify the historical loss of water from Mars.

In this work, observations from multiple instruments on the Mars Atmosphere and Volatile Evolution (MAVEN) mission are combined in order to determine the H properties in the upper atmosphere of Mars. Observations from 4 Mars Years are used to determine the variability of these properties throughout the declining activity phase of Solar Cycle 24 and the increasing activity phase of Solar Cycle 25. The properties of H atoms are examined at both perihelion season, when atmospheric circulation and regional dust storms significantly drive atmospheric variability, as well as during aphelion, when a less turbulent upper atmosphere allows for an opportunity to more directly compare annual trends with Solar Cycle.

The observations used for this investigation are described in Section 2. The results from the analysis are shown and discussed in Section 3 and concluded in Section 4. Details to the tools and methodology adopted for obtaining the resulting densities, temperatures, and escape rates from the observed parameters are provided in the Appendix.

2. Observations

Hydrogen is the most ubiquitous element in the universe (e.g., Hendrix et al., 2020), and observations of H at Mars have been made for decades (e.g., Barth et al., 1971). H atoms in the upper atmosphere of Mars resonantly scatter photons in at 1215.67 Å. MAVEN instruments include an Imaging Ultraviolet Spectrograph (IUVS) with a high-spectral resolution echelle channel that is used to make routine observations of D and H Lyman-α emissions in the upper atmosphere of Mars (McClintock et al., 2014). IUVS echelle observations examined here range from Nov 12th, 2014 (orbit 240), when the Sun was just past the maximum phase of Solar Cycle 24, through Nov 14th, 2021 (orbit 15,184), where Solar Cycle 25's activity was just beginning. This time range covers the latter perihelion portion of Mars Year (MY) 32, at Ls 233°, through two-thirds of aphelion of MY36, at Ls 124°.

H Lyman-α is a strong, extended, and ubiquitous emission near Mars (e.g., Bertaux et al., 2000 and references therein) and can emanate from martian H atoms as well as from background interplanetary (IPH) atoms (e.g., Mayyasi et al., 2017a). The IUVS instrument spectral resolution is not conducive to separating the two emissions except in cases of maximum Doppler shift between the instrument line of sight (where martian atoms are considered relatively stationary) and the IPH flow. Such occurrences of high Doppler shift between the two H atom populations are infrequent at Mars (Mayyasi et al., 2017a). To mitigate IPH contamination, only data from the dayside, disk-pointed observations, where IPH emissions are insignificant, are used for analysis of H properties.

IUVS echelle measurements of H emissions are analyzed using a data-reduction scheme described in Mayyasi et al. (2017a). A total of 3054 image sets were used for deriving H densities where the line of sight was disk-pointed. The resulting IUVS echelle observations were used to obtain a brightness of H Lyman-α emission at each of the adopted data points, along the instrument line of sight (LOS). The method used to obtain the data points from the IUVS Echelle dataset are described further in the Appendix.

The neutral atmospheric temperature at the exobase is a key metric to interpreting the variability in the properties of H atoms. The neutral temperature was derived using measurements made by the MAVEN Neutral Gas and Ion Mass Spectrometer (NGIMS) (Mahaffy et al., 2015). NGIMS measures abundances of atmospheric species in situ along the spacecraft trajectory. The temperature at Mars is considered to be isothermal above ~150 km for solar conditions used in this analysis (Krasnopolsky, 2002). An exobase temperature can therefore be directly obtained from the observed scale height of stable species (Argon and CO_2) density profiles (Mayyasi et al., 2019b). The temperatures of all atmospheric species (Ar, CO_2, H, etc.) are similar at the altitudes where these temperatures are derived due to the collisional nature of the atmosphere in this region (e.g., Mayyasi et al., 2018b). The derivation and parameterization of the exobase temperature is described further in the Appendix.

Solar irradiance impinging at the top of the martian atmosphere affects the brightness of the H emissions and is therefore a required measurement for understanding the variability in the properties of these species. The irradiance measurements were obtained by the MAVEN Extreme Ultraviolet Monitor (EUVM) in situ measurements for use with the IUVS observations (Eparvier et al., 2015; Thiemann et al., 2017). EUVM solar irradiance values at Lyman-α have a full width half max (FWHM) of 1 Å and therefore encompass the martian Lyman-α emission line of both hydrogen and deuterium atoms. Solar irradiances were converted to incident solar flux values for the H Lyman-α line center at 1215.67 Å using the relationship proposed by Emerich et al. (2005).

To derive the H abundances from the IUVS echelle observations, the measured Lyman-α spectra were reduced to provide a brightness value along a given orbital scan. A parametric representation of the neutral temperature at the exobase was then derived for the observational conditions of that orbital scan. Using the brightness along the line of sight and temperature value at the exobase, radiative transfer theory was used for the observational conditions and the solar irradiance incident along the observational line of sight to derive the H density (Chaufray et al., 2021a). A description of the radiative transfer (RT) model is provided in the Appendix.

3. Results and discussion

The purpose of this work is to investigate the solar cycle and seasonal variability of martian H properties. Multiple factors can cause additional atmospheric variability at Mars, such as: solar illumination conditions and topographical effects (e.g. Montmessin et al., 2005; Mayyasi et al., 2017b). To 'normalize' the data as much as possible, we mitigate for solar illumination conditions and topography by interpolating the derived densities to overhead illumination conditions as well as to equatorial conditions using methods described in the Appendix. The seasonal effects on H properties are then examined by comparing trends in the data during quiescent aphelion as well as during dynamic perihelion times.

During perihelion season, Mars is closest to the Sun in its orbit (perihelion is at Ls ~250°), and has maximum insolation shortly thereafter (southern summer solstice is at Ls ~270°, with insolation peak at ~280° in the southern hemisphere, due to the added factor of the angle of the Sun in the sky). During perihelion, H abundances are

strongly modified by a combination of atmospheric dynamics in the lower atmosphere, regional seasonal dust storms (e.g., Kass et al., 2016), and occasional global dust storms (e.g., MY34) (Kass et al., 2019). The events lead to enhancements in atmospheric temperature and the upwelling of water molecules (e.g., Heavens et al., 2018; Neary et al., 2020; Kleinböhl et al., 2020; Masunaga et al., 2020). Regional dust storms at Mars do not occur at exactly the same time annually, and so, trends in H properties should be evaluated separately for each year. In this work, we adopt all data points obtained between Ls 1°-180° to be at aphelion, with minimal variability in time, and all data points obtained between 181°-360° to be at perihelion, where relatively short timescale variability begins in different Mars Years. The choice of 180° as a demarcation point was made to consistently avoid any pre-perihelion variations in the data across all MYs.

The resulting normalized densities are shown in Fig. 1 as a function of solar longitude for each Mars Year. On an annual timescale, the H exobase densities can vary by over a factor 10 between aphelion and perihelion and can exhibit small time-scale fluctuations (tens of degrees in Ls). The large differences in density values between aphelion and perihelion are likely due to the coupled effects of enhanced solar insolation and dust storm activity that drive atmospheric variability at all altitudes. Similar large variations in H properties have been observed by other instruments (e.g., Bhattacharyya et al., 2015; Halekas, 2017). The large differences in orbit-to-orbit densities derived near perihelion (that exceed the uncertainties) are due to a combination of factors that include variable observational conditions along the line of sight, variable atmospheric temperatures, and the RT model assumptions. The density variations seen in the derived densities are consistent with the variability seen in the observed brightness values (e.g., Clarke et al., 2017; Mayyasi et al., 2017b). The H exobase densities consistently show less variability during the aphelion season (dynamically stable) than perihelion season. Variations within each MY are shown separately in Fig. 2 and examined.

To determine the relative importance of dust storms on H abundance in the perihelion season, three regional dust storms are examined: Types A, B and C, that typically recur annually, with varying spatial effects and temporal duration (e.g., Zurek and Martin, 1993; Kass et al., 2016; Kass et al., 2019). Mars experienced a Global Dust Storm (GDS) in MY 34, that affected the atmosphere more globally and for a longer duration than typical annual regional dust storms. During the GDS, the regional dust storms evolved into global disturbances in the lower and upper atmosphere. The regional storms onset, peak and duration observed for MYs33–35 are described in Table 1. To investigate the seasonal variability of H properties, data obtained during perihelion are analyzed in tandem with the onset, peak, and duration of regional dust storms at Mars, as shown in Fig. 2.

H densities in MY 33 (Fig. 2A) have data gaps throughout aphelion and the first half of perihelion. At perihelion, the trends with Ls show a steadily decreasing density trend following the Type B storm peak, followed by a small density enhancement near the onset and peak of the Type C dust storm.

In MY 34, Mars experienced a global dust storm. The H densities (Fig. 2B) show enhancements at the onset of the Type A storm that peak with the storm's peak and subsequently decrease. After a ~ 20° Ls data gap, density trends show an enhancement leading up to the Type B storm onset, peaking when the two regional storms overlap, followed by a decline that begins before the Type B storm peak. Densities following the Type B storm peak are enhanced from their pre-peak values, and steadily decline with Ls until onset and peak of the Type C storm where H densities increase, then decrease steadily after the storm dissipates.

Data from MY 35 is most continuous from the other Mars years shown here. H densities (Fig. 2C) increase from aphelion values during the onset of the Type A storm, and continue to increase after the storm peak. In this year, the Type A and B storms occur back-to-back. The H density trends decrease then increase again following the Type B storm peak, then decrease. H densities show a smaller peak following the Type C storm peak and then decrease to aphelion values near the end of the year.

The data available from MY 36 (Fig. 2D) span through 124° Ls and precede the expected beginning of the storm season.

While one cannot evaluate the MY33 density trends in response to the Type A storm from the dataset used in this work, one can reference MY35 trends during the Type A storm onsets and peaks that show H densities to be comparable to or larger than the observed post Type B storm peak.

In perihelion of MY33, the density drops from peak values to aphelion values in ~40° Ls. In perihelion of MY34, the localized enhancements in H densities are symmetric about their peak and span a range of ~30° Ls as seen in the 207°, 270°, 290°, and 335° Ls centered features. In perihelion of MY35, the enhancements during the Type A regional storm are symmetric about the peak densities around 250° Ls with a range of Ls ~30°. The MY35 Type B storm enhancement has a shorter range of ~20° Ls before plateauing, whereas the Type C regional storm enhancement as well as pre-Type A storm enhancement near 210° Ls span ~15° Ls.

The variability in H exobase density during perihelion is generally consistent with the onset of warmer conditions from the planet's proximity to the Sun as well as with the onset of the global Hadley cell circulation and the dust season at Mars. Density enhancements sometimes occur at the onset and/or peak of a regional dust storm, and sometimes occurs ~15°-30° in Ls later. A delay in upper atmospheric density response to storm-induced triggers may be due to a combination of regional dusk-activity, global circulation, and heating that occurs during Mars' southern summers, when insolation peaks. Furthermore, Type A dust storms typically initiate in the northern hemisphere, flow across the equator to southern latitudes during southern spring, and last between Ls 210° and 270°, affecting that atmosphere at all latitudes (Kass et al., 2016; Zurek and Martin, 1993). Pinpointing the major source of this atmospheric variability would require examining simultaneous in-situ observations from multiple atmospheric monitors at various altitudes

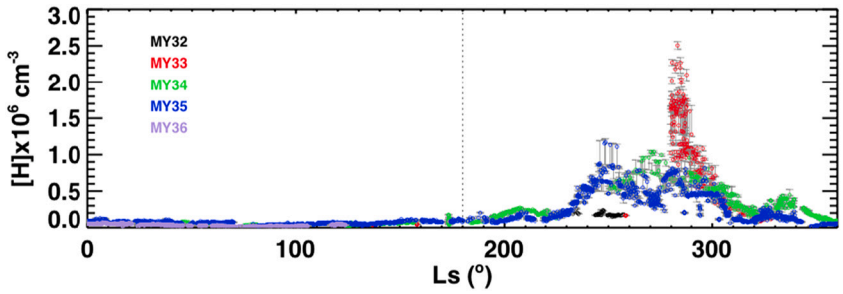

Fig. 1. Density of H at the martian exobase modeled for MAVEN echelle observations derived with a 1D RT model. The results have been scaled from the conditions of the observational line of sight to overhead Sun and equatorial conditions. The vertical dotted line at Ls 180° indicates the transition from aphelion to perihelion season adopted in this work.

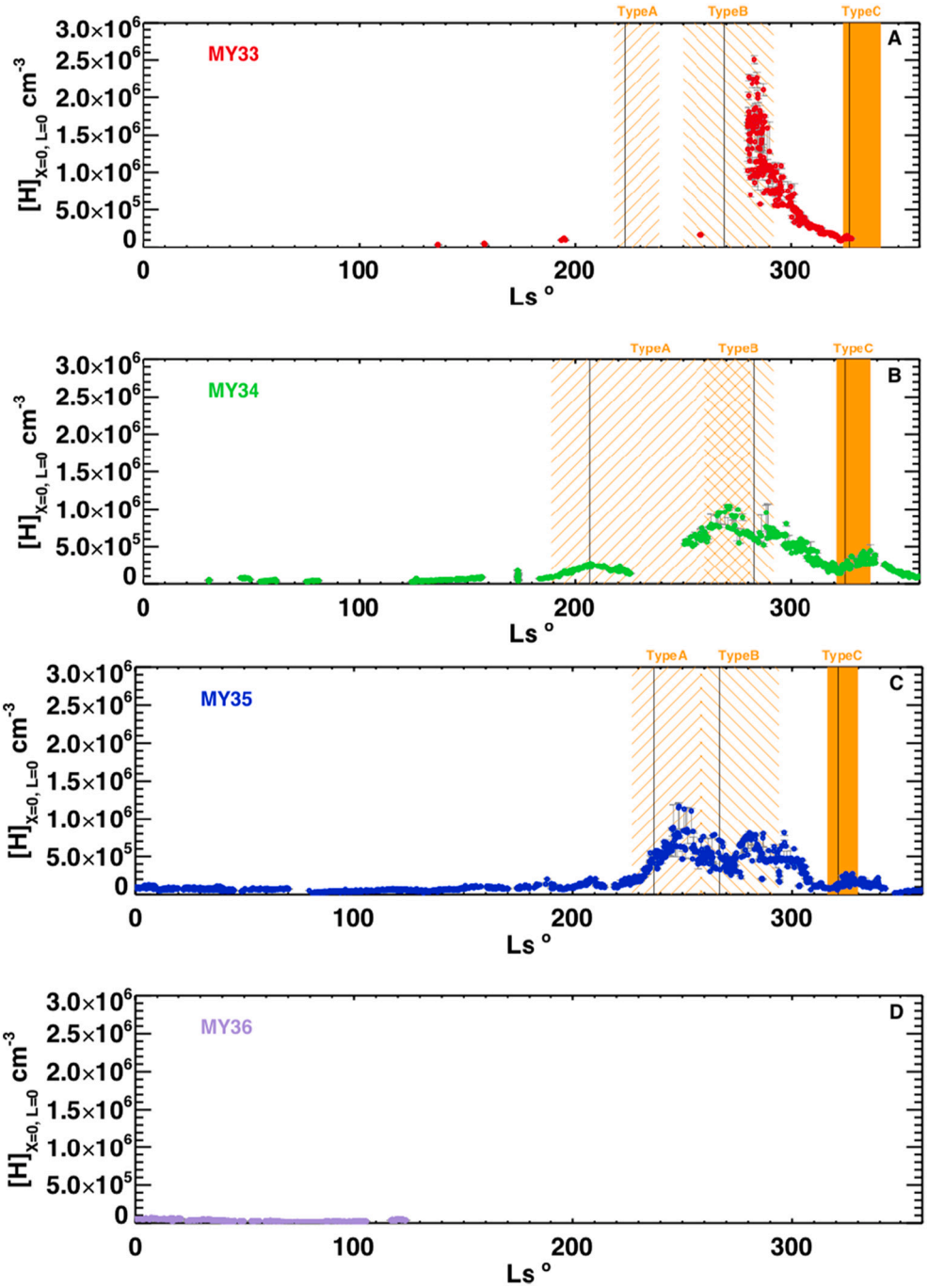

Fig. 2. H densities from MY33 (red circles, panel A), MY34 (green circles, panel B), MY35 (blue circles, panel C), and MY36 (purple circles, panel D). Yellow shaded regions denote time spans of recorded regional dust storms. Type A storms are denoted with positive-sloped hatches, Type B storms are denoted with negative sloped hatches, and Type C storms are denoted in solid yellow. The vertical black lines within each storm region denote the peak time of the storm. Storm characteristics are provided in Table 1.

at Mars and are beyond the scope of this work (Chaffin et al., 2021). These data do indicate that perihelion season increases in H density occur every Mars year, without regard to the specific level of dust storm activity.

The thermal escape rate of H atoms was calculated using the RT model derived densities at the exobase and by using an empirical fit to exobase temperature, as shown in Fig. 3. The upper atmospheric temperatures derived in this work were derived using NGIMS observations in the 40 km region above spacecraft periapsis. The atmosphere is considered to be isothermal at the altitudes adopted for this analysis; namely, ~160 km (spacecraft periapsis) through 200 km (the exobase) (e.g., Krasnopolsky, 2002). The methodology used to derive the temperature from the CO_2 scale height is described in Mayyasi et al. (2019b). The derived temperatures were normalized to overhead illumination conditions as described in the Appendix.

The resulting temperatures, shown in Fig. 3, show repeatable annual variability that is attributed, in part, to the spacecraft periapsis precession as well as to variability in the exobase altitude driven by the lower atmosphere (Jakosky et al., 2017). While the exobase altitude may change from orbit-to-orbit (between ~150–200 km), the RT model assumption of exobase altitude at 200 km is still a valid representation of the atmosphere as both H densities and temperatures do not vary significantly between 150 and 200 km (e.g., Matta et al., 2013).

To quantify the aphelion to perihelion variation in global thermal conditions, temperature averages were used for each Mars Year during aphelion season (Ls = 0°–180°) and perihelion season (181°–360°) to smooth out the observational variations and to constrain an empirical fit to the data. The parameterized exobase temperature at SZA =

Table 1
Seasonal span of classical regional dust storms and the GDS for MYs 33–35. Ls peak is derived from time-evolving zonal averaged temperatures at 50 Pa.

	Storm	Start Ls / Date	~Peak Ls / Date	End Ls / Date
MY33	A	218° / Sep 6, 2016	223° / Sep 15, 2016	239° / Oct 10, 2016
	B	250° / Oct 27, 2016	269° / Nov 26, 2016	292° / Jan 2, 2017
	C	324° / Feb 26, 2017	327° / Mar 3, 2017	342° / Mar 31, 2017
	GDE*	189° / Jun 6, 2018	207° / Jul 7, 2018	270°-281° / Oct 14–Nov 3, 2018
MY34	B	260° / Oct 1, 2018	283° / Nov 6, 2018	292° / Nov 20, 2018
	C	321° / Jan 8, 2019	325° / Jan 16, 2019	337° / Feb 6, 2019
MY35	A	227° / Jun 25, 2020	237° / Jul 12, 2020	259° / Aug 16, 2020
	B	258° / Aug 13, 2020	267° / Aug 28, 2020	294° / Oct 10, 2020
	C	316° / Nov 17, 2020	321° / Nov 26, 2020	330° / Dec 12, 2020

* The start date assumes similar criteria as non-GDE storms (Kass et al., 2019).

0° conditions adopted for this work accounts for variations due to season and solar cycle and is consistent with global temperatures derived from other works (e.g., Forbes et al., 2008; Bougher et al., 2009). The day-to-day variability in the atmospheric temperatures at Mars can be large and further enhanced during dust storms or transient solar events (e.g., Mayyasi et al., 2018a; Jain et al., 2021). A discussion of the uncertainties in the parameters derived in this work and their implication is included in the Appendix.

The empirical fit to exobase temperature and the derived H exobase density were used to determine the thermal escape rate of H atoms using the Jeans escape formulation (described further in the Appendix). As demonstrated in Fig. 3, there is significant seasonal variability in the escape rate across the MAVEN mission timeline. Within one full Mars Year, the thermal escape rate extrema differ by over two orders of magnitude between aphelion and perihelion, as is the case for MY33, MY34, and MY35.

Determinations of the abundances of H atoms in the atmosphere of Mars using radiative transfer theory are sensitive to the ambient temperature. In Sep 2018, a Coronal Mass Ejection and Solar Flare impacted Mars while MAVEN was in orbit (Lee et al., 2018). IUVS echelle measurements recorded a brightness enhancement of ~25% in H Lyman-α emissions and NGIMS measurements recorded a temperature enhancement of ~80 K during the few days of the solar storm impact. For these observations, the derived H exobase densities was found to increase by 25% and the escape rate was enhanced by a factor of 5 (Mayyasi et al., 2018a).

As a best attempt to adopt complex radiative transfer theory assumptions to produce density derivations, the RT model utilizes empirical solar irradiance and brightness values for each data point along the observational line of sight. The simplification introduced by adopting empirical averages for temperatures may introduce additional uncertainties in the derived exobase density, where temperatures may fluctuate by a few tens of degrees over short timescales. A more in-depth and systematic derivation of day-to-day variability of ambient temperatures and upper atmospheric properties at Mars is an ongoing investigation and has been preliminarily quantified in Chaufray et al. (2021a).

The seasonally averaged H exobase temperature, density, thermal escape rate, and global escape rates derived from MAVEN observations are shown in Fig. 4. Seasonal averages smooth out the shorter timescale variability and highlight the effects of a variable solar cycle. The minimum of Solar Cycle 24 occurred near Sep 2019, at Ls ~80° in MY35. Therefore, the decreasing activity phase of Solar Cycle 24 overlaps with MAVEN observations in perihelion season of MY32, all of MYs 33–34, and the first third of aphelion season in MY35. The increasing activity phase of Solar Cycle 25 overlaps with MAVEN observations in the remaining two-thirds of aphelion season and all perihelion season of MY35, and the aphelion season of MY36. We note that MY36 data coverage went up to Ls 124°, just prior to a projected enhancement in exobase temperature that leads into perihelion, as seen in the thermal trends from previous Mars Years.

The seasonally-averaged exobase temperature (Fig. 4A) decreases from solar moderate conditions of MY32 to solar minimum conditions of MY34, and increases as the solar cycle becomes more active in MY35 during perihelion. During aphelion, the averaged exobase temperature

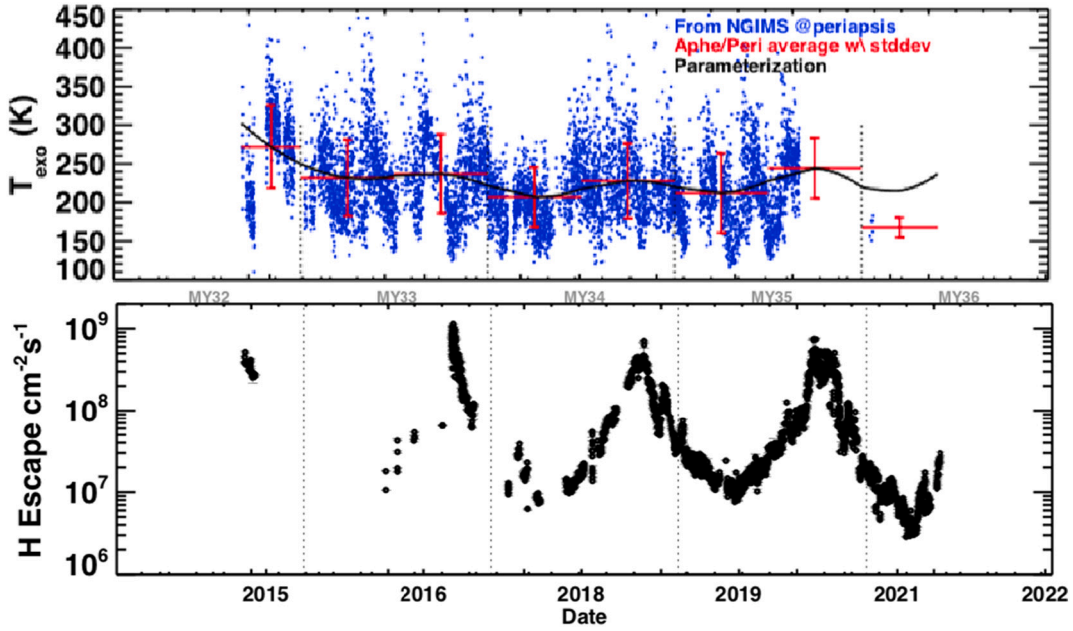

Fig. 3. (Top panel) The NGIMS-derived temperatures extrapolated to SZA = 0° (blue dots), averaged over aphelion and perihelion seasons (horizontal red lines) with their standard deviation about the mean (vertical red lines) that are used to constrain the empirical fit (black) for exobase temperature. The temperature fit is used to derived the H thermal escape rates (Bottom panel) for SZA = 0° conditions.

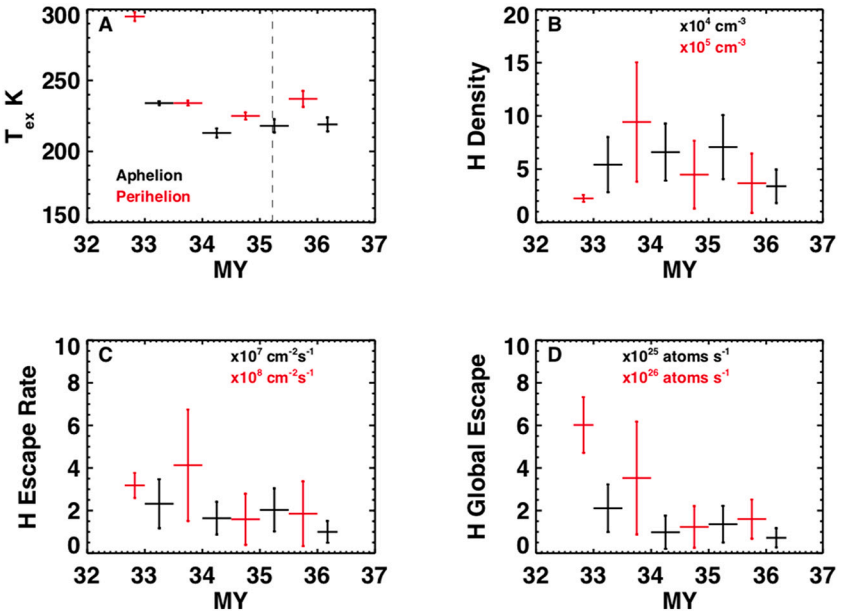

Fig. 4. Seasonally averaged properties of temperature (A), exobase density (B), thermal escape rate (C), and global escape rate (D) for H atoms at Mars for aphelion-averaged values (black) and perihelion-averaged values (red). The length of the horizontal line spans the Ls where data are available (partial for MY32 perihelion and MY36 aphelion). Vertical error bars in temperature reflect the standard deviation in the empirical fit. Vertical error bars in H density, thermal escape, and global escape rates are propagated from the uncertainties in the data (e.g., Mayyasi et al., 2017a). The vertical dashed line in panel A denotes the reference solar minimum point for Solar Cycle 24, at 80° Ls of MY35. (For interpretation of the references to color in this figure legend, the reader is referred to the web version of this article.)

decreased from MY33 to MY34 and begins to increase again in MY35 and MY36.

The H exobase density (Fig. 4B) increases with decreasing solar activity from MY32 to MY33 during perihelion. The perihelion densities decrease in MY34 then continue to decrease with increasing solar activity in MY35. During aphelion, the seasonally averaged H exobase densities increase with decreasing solar activity, and decrease with increasing solar activity. With the exception of MY34 perihelion trends, the seasonally-averaged H exobase densities vary inversely with solar activity, likely due to variations in temperature. The inverse relationship between H exobase density and temperatures is consistent with findings from previous studies that examine diffusion theory of lighter atoms through an atmosphere of heavier species (Krasnopolsky, 2002). The martian atmosphere at ~200 km is predominantly composed of CO_2, O, N_2, CO, O_2 and Ar (Mahaffy et al., 2015). Enhanced solar irradiance at Mars results in overall heating and expansion of the atmosphere. As these dominant species expand with increasing solar irradiance and subsequent heating, lighter species such as H, encounter increased collision rates that slow their diffusion to higher altitudes. Studies have shown that during a transient space weather event that spiked thermospheric temperatures by 15% and 40%, the H densities decreased by 8% and 25%, respectively (Mayyasi et al., 2018a). Conversely, cooler temperatures result in a smaller scale height for heavier species and a relatively deflated atmosphere that reduces collisions with the lighter species at exobase altitudes and facilitates the diffusion of H atoms to higher altitudes. The exceptional behavior of MY34 perihelion may be driven by the global dust events that affected mixing and diffusion of H atoms to higher altitudes (e.g., Chaffin et al., 2021).

The seasonally-averaged H thermal escape rate (Fig. 4C) decreases with solar activity in solar cycle 24, from MY33 through MY34, then increases with increasing solar activity during MY35 for perihelion. The aphelion-averaged escape rate also decreases with solar activity from MY33 to MY34, then increases in MY35 with the enhanced solar activity. The perihelion-averaged MY32 and aphelion-averaged MY36 escape rates are lower than expected from trends formed by other MY seasons, and may be due to the incomplete dataset available from those seasons (233°-360° Ls for MY3 and 0°-124° Ls for MY36), where projected trends would lead to higher temperatures and therefore higher escape rates. Aside from these partial seasonal representations, the seasonally-averaged H thermal escape rate correlates with solar activity.

A global escape rate for each of the aphelion and perihelion averaged conditions was extrapolated from the thermal escape rate for H. The escape flux per unit area falls off from 0° to 180° SZA with the corresponding decrease in exospheric temperature. As a first approximation, the NGIMS temperature profile with SZA is used with the normalization relation for density profile with SZA (described in Appendix) to encompass all solar illumination conditions. The calculated escape fluxes were then integrated over the planet for all SZA to obtain a global rate. The global escape rate is roughly ½ the rate that would be obtained by integrating the sub solar escape rate across the globe.

The resulting global escape rate (Fig. 4D) correlates with solar activity, decreasing during the declining phase of Solar Cycle 24 and increasing with the increasing activity phase of Solar Cycle 25 for perihelion. During aphelion, the global escape rate shows similar trends with solar activity as in perihelion with the exception of aphelion of MY36. This is likely due to the partial data available for that season. Similar to the discussion provided for thermal escape rate, the temperature for the remaining aphelion season of MY36 is projected to increase, as is the solar activity, causing the resulting aphelion averaged global escape rate to increase. Additionally, when considering the H thermal escape rate in perihelion of MY32 to be lower than expected dur to partial data coverage, the subsequent global escape rate for MY32 perihelion may be higher than the average value derived here for the partial seasonal.

Further enhancements in solar activity from a stronger solar cycle will likely result in larger variations in the seasonal properties of H atoms. Observations acquired during a stronger solar maximum than available with the present MAVEN observations will be required to better quantify how such conditions could affect H escape at Mars.

4. Conclusion

Observations obtained with MAVEN were used to derive trends in the upper atmospheric properties of H atoms at solar moderate-to-minimum conditions as well as with season. The properties include exobase densities and temperatures that were then used to calculate thermal and global escape rates.

Significant seasonal variability was found in the derived properties of H atoms at the exobase from year to year. H densities at perihelion were consistently higher than at aphelion and showed variability in response to regional dust storms onset and peaks, with a duration range of 15°-40° Ls. Occasional density and escape rate enhancements during

perihelion were offset in time from a regional storm trigger likely due to a combination of dust storm and atmospheric circulation effects. During the year of the GDS, H densities at perihelion were not significantly enhanced above their values in adjacent years.

The persistent year-to-year increase in H density around perihelion is consistent with a measured increase in high altitude H_2O found by IR solar occultation data (Aoki et al., 2019; Vandaele et al., 2019; Fedorova et al., 2020; Stone et al., 2020; Belyaev et al., 2021) and this occurs in phase with the known strong Hadley cell circulation pattern (Montmessin et al., 2017; Neary et al., 2020; Shaposhnikov et al., 2019). Increased dust in the atmosphere contributes to increased temperatures and increased circulation, thus the effects of atmospheric dynamics and dust storm activity are linked. The weak response of H densities to the MY 34 global dust storm may be due in part to the enhanced temperatures that suppress the diffusion of H atoms to higher altitudes, resulting in a lower abundance of H atoms at the exobase. It is also possible that since the global dust event occurred well before perihelion the global Hadley circulation pattern was not yet established, leading to a relatively lower increase in upper atmospheric H density.

During aphelion, variations in the H exobase densities and escape rates were compared across solar activity periods that include near-maximum through minimum phase of Solar Cycle 24 as well as the beginning of Solar Cycle 25. Aphelion H densities at the exobase increased as the Sun became less active, then decreased as the Sun became more active. The aphelion thermal and global H escape rates decreased with decreasing solar activity and increased with increasing solar activity.

The H density values obtained in this work are consistent with previous findings by Rosetta, Mars Express, Mariners 6 & 7, as well as Mars-3 mission data for solar extreme conditions that span ~0.06–4 $\times$ 10^5 cm^{-3} (Anderson and Hord, 1971, 1972; Dementyeva et al., 1972; Galli et al., 2006; Chaufray et al., 2008; Feldman et al., 2011). The H thermal escape rate obtained in this work is consistent with findings using lower spectral resolution MAVEN data that range between 0.6 and 8.8 $\times$ 10^8 cm^{-2} s^{-1} for available data in MY32 through end of aphelion in MY33 (Chaffin et al., 2018). The thermal escape rate of H, averaged over all data points (for all seasons) is 8.9 $\times$ 10^7 cm^{-2} s^{-1}. This finding supports that of previous works where averaged martian conditions were used to obtain a thermal escape rate of 5.4 $\times$ 10^7 cm^{-2} s^{-1} (Yung et al., 1988). The H global escape rate results are consistent with findings obtained with Mars Express data and modeling analyses that showed a seasonal variation of ~0.1–6 $\times$ 10^{26} atoms s^{-1} during MY28 and 29, that similarly overlapped with moderate-to-minimum decreasing activity phase of Solar Cycle 23 (Chaufray et al., 2021b).

The mean global escape rate found in this analysis, averaged over all data points, is 1.4 $\times$ 10^{26} atoms s^{-1}. This extrapolates to a global equivalent layer of water ~1.2 m deep, lost over four billion years. The extreme values of escape rate obtained from the observations span between 2.9 $\times$ 10^6 cm^{-2} s^{-1} and 7.5 $\times$ 10^8 cm^{-2} s^{-1}. These extreme values correspond to a global escape rate of 1.9 $\times$ 10^{24} and 1.36 $\times$ 10^{27} atoms s^{-1}. Using these extreme values as references, the global equivalent layer of water, lost over 4 billion years ranges between ~2 cm and ~ 13 m deep. While these extreme values are limits derived from this work for MAVEN observations made between solar moderate and solar minimum conditions, they can help constrain further investigations as to the loss of water from Mars (e.g., Jakosky, 2021).

The variability in H properties due to variations in solar activity indicate a solar activity dependence. However, this solar cycle dependence is dwarfed by seasonal effects that significantly enhance H abundances and escape rates to space during perihelion seasons of each MY. As MAVEN continues to orbit Mars, more IUVS data will become available during the peak of Solar Cycle 25 for future analysis. The results suggest that solar activity can affect the rate of water loss from the planet, and should be quantified during a stronger solar cycle to more completely assess the effects of solar cycle extrema on water escape and subsequent extrapolations of primordial water content of Mars.

Declaration of Competing Interest

None.

Acknowledgements

The authors would like to thank two anonymous reviewers for their helpful suggestions. The MAVEN data used in this study are available on the NASA PDS Atmospheres Node at: https:// pds-atmospheres.nmsu.edu/data_and_services/atmospheres_data/MAVEN/maven_main.html. IUVS echelle level1a v13 data were used. This work generated high-level data products (hydrogen densities and escape rates derived from PDS products) which will be archived in the FAIR-compliant CU Scholar Repository at (URL pending). This work was funded, in part, by NASA contract #1000320450 from the University of Colorado to Boston University, and by NASA grant #80NSSC18K0266.

Appendix A. Tools and methods

A.1. Data reduction

The data measured by MAVEN IUVS echelle consists of a set of images, obtained for each orbit, for thousands of orbits. For purposes of analyzing the H Lyman-α emissions, only observations in which the instrument was pointed at the planetary disk were used (to minimize contamination by interplanetary H Lyman-α emissions). For each of the observations, images were co-added across the image set to produce a single image which was then used to derive a spectrum to optimize the signal to noise. The observational parameters for each image set were also co-added to provide one representative line-of-sight for the co-added spectrum.

The co-added spectra were then reduced to provide a brightness value for H Lyman-α in Rayleigh (Mayyasi et al., 2017a). The co-added observational parameters for the line-of-sight include latitude, and SZA of the point where the line of sight intersect the planet disk for each image in a set. The range of where the line-of-sight intersects with the planetary disk typically spans a few degrees in latitude and SZA for the individual images in a set. These parameters are co-added to provide one representative observational geometry to represent the co-added spectrum. Testing this methodology of co-adding images and their geometry against image-by-image analysis was done and found to be similar.

The co-added brightness and its associated uncertainty (described at length in Mayyasi et al. (2017a)), co-added line-of-sight parameters, and an exospheric temperature are then provided to a radiative transfer model to produce a density value at the exobase above the location of the observational point on the planetary disk.

A.2. Temperature parameterization

The neutral temperature in the upper atmosphere of Mars does not vary significantly above the exobase and a single temperature is used for all

species at that altitude (Krasnopolsky, 2002). To derive a temperature that is representative of the ambient conditions of the MAVEN IUVS disk-pointed observations of H, NGIMS in-situ measurements of neutral species abundances were used. The CO_2 density, observed as a function of altitude within 40 km of the spacecraft periapsis, provides the exponentially decreasing molecular abundances with increasing altitude (Mahaffy et al., 2015). The CO_2 scale height above the spacecraft periapsis (~160–180 km) is used to obtain the exobase temperature, in a method that is described in Mayyasi et al. (2019b). The exobase temperature provided to the RT model is then used to construct a temperature profile with altitude (e.g., Krasnopolsky, 2002).

To normalize the observations to overhead Sun conditions, the exobase temperatures (T_{exo}) derived from the NGIMS data were parameterized as a function of SZA for the mission-long trends in dayside temperatures (SZA < 90°). The resulting parameterized fit for T_{exo} with SZA, shown in Fig. A1, is consistent with that obtained by other investigations (Stone et al., 2020; Mayyasi et al., 2019a) which used a briefer MAVEN data timeline. The parameterization was used to obtain an overhead illumination (SZA = 0°) value for T_{exo}. The SZA = 0° value of the T_{exo} fit was then scaled to reflect seasonal and solar activity, as shown in Fig. 3 (top panel).

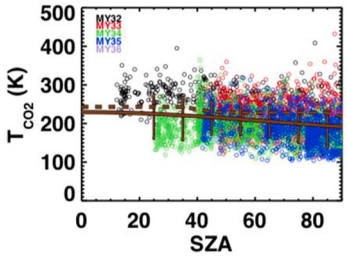

Fig. A1. Exobase temperature derived from NGIMS measurements of CO_2 scale heights made on the dayside (SZA < 90°) from 7 years of MAVEN observations. Data from MYs 32, 33, 34, 35 and 36 are shown in circles colored black, red, green, blue, and purple, respectively. The standard deviation in temperature, derived from 10° SZA bin averages, is shown in vertical brown bars. The best fit to the averages is shown as a solid brown line. The fit is compared with that of other workers (brown dotted line) (e.g., Stone et al., 2018). (For interpretation of the references to color in this figure legend, the reader is referred to the web version of this article.)

A.3. Radiative transfer (RT) model

A radiative transfer technique is used to derive the H densities from the IUVS Echelle brightness measurements using a 1-dimentional (1D) model that uses a forward approach (e.g., Chaufray et al., 2021a, and references therein). The model generates a temperature profile with altitude, based on the NGIMS-derived values near spacecraft periapsis. The atmospheric temperature at Mars can be variable with altitude below the homopause (~60–140 km) (e.g., Slipski et al., 2018), yet is expected to be fairly constant at thermospheric altitudes (~140–200 km) (Krasnopolsky, 2002). The RT model assumes a homopause at 80 km altitude, below which all Lyman-α photons are absorbed, and an exobase at 200 km altitude. The exobase temperature is expected to vary with season, local time, and solar forcing (e.g., Jain et al., 2021) and these variations have been captured by the empirical fits to the NGIMS data.

The model also assumes an H density profile with altitude (e.g., Anderson, 1974; Bhattacharyya et al., 2020). Using the location of the spacecraft and the observational LOS, the model then uses a Monte Carlo approach to simulate the volume emission rate of H along the LOS. The model assumptions include adopting a thermal-only component of the atmosphere, (that is applicable to the observations used in this analysis), a symmetric atmosphere with CO_2, absorption considerations for optically thick H emissions, and an angle-dependent partial frequency redistribution function. The solar Lyman-α flux along the LOS linearly affects the Lyman-α emission by H atoms. The RT model accounts for this by using measurements obtained in-situ at Mars by the Extreme Ultraviolet Monitor (EUVM) (Eparvier et al., 2015).

The RT model produces a library of H density distributions with altitude, and simulates the brightness of each distribution at a range of ambient temperatures (e.g., Fig. 2 in Bhattacharyya et al., 2020). The best-fit distribution for H atoms returned by the RT model is the one that produces a brightness profile that best matches the observed brightness at the given temperature. The model assumes a symmetric atmosphere and converts the best-fit distribution along the observational LOS into a density profile for H with altitude at the observation point on the disk identified by the LOS. The H density at the exobase altitude (200 km) is the provided as output from the RT model to be used as a metric for this analysis. Model density distributions and atmospheric assumptions have been previously described and the sensitivity of the model results to assumed parameters and inputs have been characterized in previous works (Bhattacharyya et al., 2020; Chaufray et al., 2021a).

A.4. Normalizing to overhead sun

The modeled H densities show a dependence on solar illumination conditions, determined by the SZA. To account for those variations, the densities retrieved during aphelion conditions (when seasonal variability is at a minimum) were used to identify the trends in the densities with SZA, as shown in Fig. A2. Perihelion densities show similar trends with SZA but have much larger spread due to additional atmospheric drivers and so we refrain from using those data points to derive trends with SZA. The densities were averaged over 5° bins in SZA, and a best fit curve was determined for each species that best represented the average trends. The functional form of the fit is:

$$[H]\left(cm^{-3}\right) = \frac{5.0 \times 10^4}{cos(\chi)^{0.2}} \tag{A1}$$

where *[H]* is the hydrogen density in cm^{-3}, and χ is the SZA. This functional form was used to 'normalize' the densities to overhead illumination (aka zenith) conditions, when the SZA = 0°. Corrections to overhead solar illumination conditions mostly affected data points at larger SZA. The density correction to overhead Sun conditions was <7%, on average, for data at SZA <65°, and up to 36% for data at SZA > 65°.

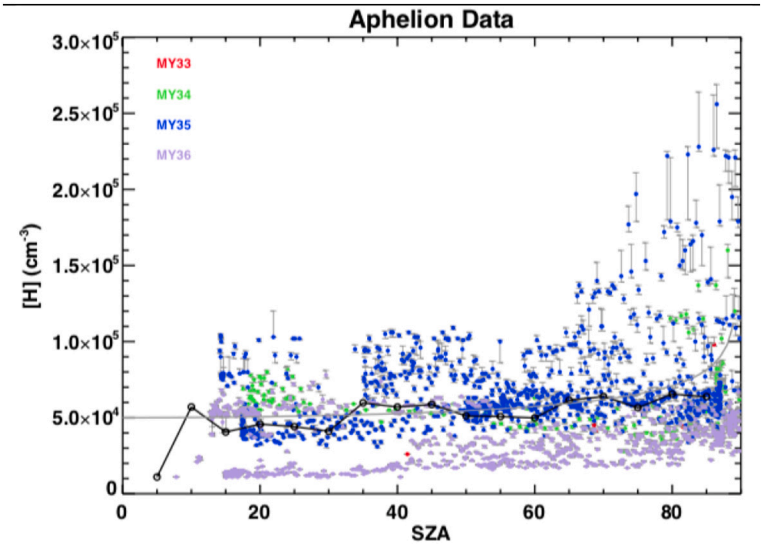

Fig. A2. Aphelion densities for H as a function of SZA. The modeled densities (color coded by Mars Year, specified in the legends) were averaged over 5° SZA bins (black circles and solid lines) to determine the average trend in density with illumination conditions. The trend was used to determine a functional fit represented by Eq. A1, shown as grey solid line across the data points. Vertical thin grey lines represent the uncertainty in the model results for each data point.

A.5. Normalizing to equatorial conditions

The martian atmosphere undergoes large variations with seasons related to dust activity. To minimize the added effects of dust variability, that occur mostly around the perihelion season, only aphelion data points were used to examine trends in modeled values with latitude. The results are shown in Fig. A3 and utilize data that has been normalized to overhead Sun conditions, using Eq. A1.

The trend in H densities with latitude was determined by smoothing averaged values, obtained for the densities over each 5° bin. The smoothed fit was then used to normalize densities to equatorial values. The variability with latitude was <25% of the equatorial value for H densities.

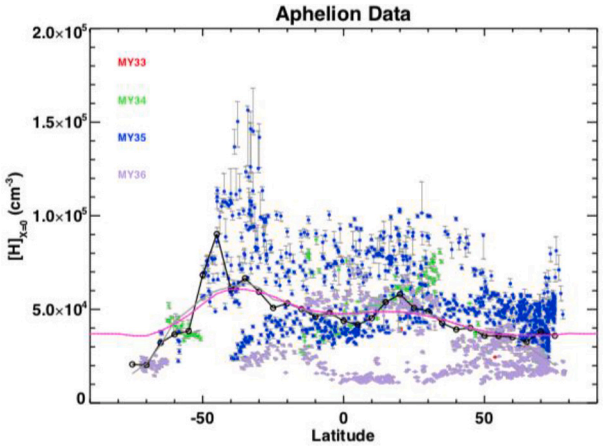

Fig. A3. Aphelion H densities as a function of latitude. These modeled densities (color coded by MY shown in the legend) have been normalized to SZA = 0°. The data points were averaged over 5° latitude bins (black circles and solid lines) to determine the average trend in density with latitude. The trends were smoothed to provide the fits (pink solid lines) to latitudinal variability and are not represented by a functional form. Vertical thin grey lines represent the uncertainty in the model results for each data point. (For interpretation of the references to color in this figure legend, the reader is referred to the web version of this article.)

The data before and after the SZA and latitudinal corrections are shown in Fig. A4 and the latter is shown in Fig. 1.

A.6. Escape rate

The escape rate for H atoms in the upper atmosphere of Mars is derived from the standard Jeans Escape formulation (e.g., Hunten, 1982; Sanchez-Lavega, 2015):

$$H\ escape = \frac{1}{2\sqrt{\pi}}[H] \times e^{-\tau} \times V_{th} \times (\tau + 1) \tag{A2}$$

$$V_{th} = \frac{2k_b T_{exo}}{m} \tag{A3}$$

$$\tau = \frac{GMm}{k_B T_{exo} h_{exo}} \tag{A4}$$

where k_b is the Boltzmann's constant, m is the mass of a Hydrogen atom, G is the universal gravitational constant, M is the mass of Mars, and h_{exo} is the exobase altitude, taken here to be 200 km.

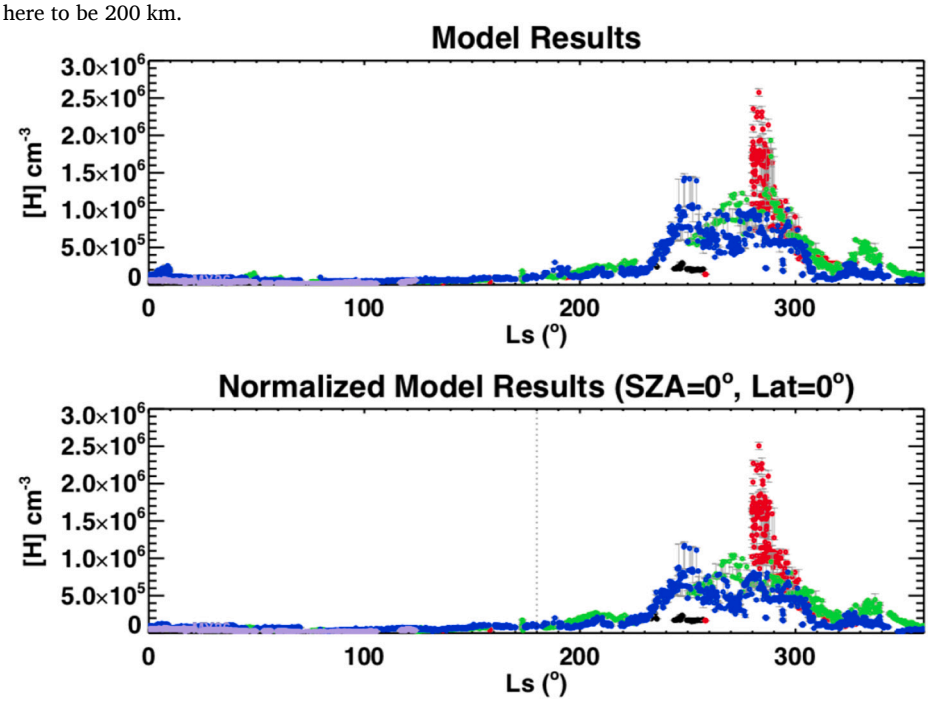

Fig. A4. Modeled densities for H before correction (top row) and after correction (bottom row). Densities are corrected by normalizing the data points to overhead illumination (SZA = 0°) and equatorial conditions (latitude = 0°). Data from each MY is color coded. Vertical thin grey lines denote uncertainties in the modeled values. A vertical dotted line in the normalized values at 180° Ls demarks aphelion from perihelion season.

A.7. Uncertainties in the derived parameters

Measurements of IUVS H Lyman-α emissions and NGIMS CO_2 scale heights are used to derive the brightness and ambient temperature of H atoms along a line of sight. These derived values are used with measured EUV solar irradiance and a radiative transfer model in order to derive the H abundances at the exobase altitude along the line of sight. The densities and the temperatures are combined to derive H thermal escape rates for overhead illumination conditions as well as global escape rates at all SZAs, assuming the diurnal variations of density and temperature across the planet as described above.

The uncertainties in the brightness values are derived from the background noise in the reduced spectrum and are <15% for individual spectra of bright emissions such as H Lyman-α (Mayyasi et al., 2017a). When co-added for improved signal to noise, as done here, the uncertainty due to noise in the spectral signal drops to <4%. The uncertainties in the brightness values are smaller than the uncertainty in the absolute calibration of the instrument, which is ~25% and is stable over time (Mayyasi et al., 2017). This paper describes changes in H properties in the upper atmosphere of Mars and thus the plotted error bars do not include this value.

The uncertainties propagated by the radiative transfer code, due to uncertainties in the input parameters and model assumption, have been discussed in (Chaufray et al., 2021a).

The measurement uncertainties in the NGIMS CO_2 densities are typically small (<20%) near spacecraft periapsis, where these densities are used to derive exobase temperatures (Mahaffy et al., 2015). In addition, the assumed temperature values are fit to averaged empirical data. The seasonal averaging of derived temperatures has a standard deviation of ~80 K. Such a spread in exobase temperature is estimated to affect the derived densities by ~25%, and the derived escape rates and global escape rates by a factor of ~5 (e.g., Mayyasi et al., 2018a).

References

Alday, J., et al., 2021. Isotopic fractionation of water and its photolytic products in the atmosphere of Mars. Nature Astronomy. https://doi.org/10.1038/s41550-021-01389-x.

Anderson, D.E., Hord, C.W., 1971. Mariner 6 and 7 ultraviolet spectrometer experiment: Analysis of hydrogen Lyman alpha. J. Geophys. Res. 76, 6666–6673.

Anderson, D.E., Hord, C.W., 1972. Correction: "Mariner 6 and 7 ultraviolet spectrometer experiment: Analysis of hydrogen Lyman-alpha data" [J. Geophys. Res., Vol. 76, p. 6666–6673 (1971)]. J. Geophys. Res. 77, 5638.

Aoki, S., Nakagawa, H., Sagawa, H., Giuranna, M., Sindoni, G., Aronica, A., Kasaba, Y., 2015. Seasonal variation of the HDO/H2O ratio in the atmosphere of Mars at the middle of northern spring and beginning of northern summer. Icarus 260, 7–22. https://doi.org/10.1016/j.icarus.2015.06.021.

Aoki, S., Vandaele, A.C., Daerden, F., Villanueva, G.L., Liuzzi, G., Thomas, I.R., Erwin, J. T., Trompet, L., Robert, S., Neary, L., Viscardy, S., Clancy, R.T., Smith, M.D., Lopez-Valverde, M.A., Hill, B., Ristic, B., Patel, M.R., Bellucci, G., Lopez- Moreno, J.-J., the NOMAD team, 2019. Water vapor vertical profiles on Mars in dust storms observed by TGO/NOMAD. J. Geophys. Res. https://doi.org/10.1029/2019JE006109.

Barth, C., Hord, C., Pearce, J., Kelly, K., Pearson, G., Stewart, I., 1971. Mariner 6 and 7 ultraviolet spectrometer experiment: upper atmosphere data. J. Geophys. Res. 76, 10.

Belyaev, D., Federova, A., Rrokhimovskiy, A., Alday, J., Montmessin, F., Korablev, O., Lefèvre, F., Patrakeev, A., Olsen, K., Shakun, A., 2021. Revealing a high water abundance in the upper mesosphere of mars with ACS onboard TGO. J. Geophys. Res. https://doi.org/10.1002/essoar.10506560.2.

Bertaux, J.-L., Fonteyn, D., Korablev, O., Chassefiere, E., Dimarellis, E., Dubois, J.P., Hauchecorne, A., Cabane, M., Rannou, P., Levasseur-Regourd, A.C., Cernogora, G., Quemerais, E., Hermans, C., Kockarts, G., Lippens, C., De Maziere, M., Moreau, D., Muller, C., Neefs, B., Simon, P.C., Forget, F., Hourdin, O. Talagrand, Moroz, V.I., Rodin, A., Sandel, B., Stern, A., 2000. The study of the Martian atmosphere from top to bottom with SPICAM light on Mars Express. Planetary and Space Science 48, 1303–1320.

Bhattacharyya, D., Clarke, J.T., Bertaux, J.-L., Chaufray, J.-Y., Mayyasi, M., 2015. A strong seasonal dependence in the Martian hydrogen exosphere. Geophys. Res. Lett. 42 https://doi.org/10.1002/2015GL065804.

Bhattacharyya, D., Chaufray, J.Y., Mayyasi, M., Clarke, J.T., Stone, S., Yelle, R., Pryor, W., Bertaux, J.L., Deighan, J., Jain, S.K., Schneider, N.M., 2020. Two-dimensional model for the martian exosphere: applications to hydrogen and

deuterium Lyman α observations. Icarus 339. https://doi.org/10.1016/j.icarus.2019.113573.
Bougher, S.W., McDunn, T.M., Zoldak, K.A., Forbes, J.M., 2009. Solar cycle variability of Mars dayside exospheric temperatures: model evaluation of underlying thermal balances. Geophys. Res. Lett. 36, L05201. https://doi.org/10.1029/2008GL036376.
Chaffin, M.S., Chaufray, J.-Y., Stewart, I., Montmessin, F., Schneider, N.M., Bertaux, J.-L., 2014. Unexpected vari- ability of Martian hydrogen escape. Geophys. Res. Lett. 41, 314–320. https://doi.org/10.1002/2013GL058578.
Chaffin, M.S., Deighan, J., Schneider, N.M., Stewart, A.I.F., 2017. Elevated atmospheric escape of hydrogen from Mars induced by high-altitude water. Nat. Geosci. 10, 174–178. https://doi.org/10.1038/ngeo2887.
Chaffin, M.S., Chaufray, J.Y., Deighan, D., Schneider, N.M., Mayyasi, M., Clarke, J.T., et al., 2018. Mars H escape rates derived from MAVEN/IUVS Lyman alpha brightness measurements and their dependence on model assumptions. Journal Geophysical Research: Planets 123. https://doi.org/10.1029/2018JE005574.
Chaffin, M., Kass, D., et al., 2021. Martian water loss to space enhanced by regional dust storms. Nature Astronomy 5, 1036–1042.
Chaufray, J.-Y., Bertaux, J.-L., Leblanc, F., Merais, E. Qu, 2008. Observation of the hydrogen corona by SPICAM on Mars Express. Icarus 195, 598–613. https://doi.org/10.1016/j.icarus.2008.01.009.
Chaufray, J.-Y., Mayyasi, M., Chaffin, M., Deighan, J., Bhattacharyya, D., Clarke, J., et al., 2021a. Estimate of the D/H ratio in the Martian upper atmosphere from the low spectral resolution mode of MAVEN/IUVS. J. Geophys. Res. Planets 126. https://doi.org/10.1029/2020JE006814 e2020JE006814.
Chaufray, J.-Y., Gonzalez-Galindo, F., Lopez-Valverde, M., Forget, F., Quémerais, E., et al., 2021b. Study of the hydrogen escape rate at Mars during Martian years 28 and 29 from comparisons between SPICAM/Mars express observations and GCM-LMD simulations. Icarus 353, 113498. https://doi.org/10.1016/j.icarus.2019.113498.
Clarke, J.T., 2018. Dust-enhanced water escape. Nat. Astronomy 2, 114–115. https://doi.org/10.1038/s41550-018-0383-6.
Clarke, J.T., Bertaux, J.-L., Chaufray, J.-Y., Gladstone, G.R., Quemerais, E., Wilson, J.K., Bhattacharyya, D., 2014. A rapid decrease of the hydrogen corona. Geophys. Res. Lett. 41, 8013–8020. https://doi.org/10.1002/2014GL061803.
Clarke, J.T., et al., 2017. Variability of D and H in the Martian upper atmosphere observed with the MAVEN IUVS echelle channel. J. Geophys. Res. Space Physics 122. https://doi.org/10.1002/2016JA023479.
Dementyeva, N.N., Kurt, V.G., Smirnov, A.S., Titarchuk, L.G., Chuvahin, S.D., 1972. Preliminary results of measurements of UV emissions scattered in the Martian upper atmosphere. Icarus 17, 475–483.
Emerich, C., Lemaire, P., Vial, J.C., Curdt, W., Schule, U., Wilhelm, K., 2005. A new relation between the central spectral solar H I Lyman α irradiance and the line irradiance measured by SUMER/SOHO during the cycle 23. Icarus 178, 429–433.
Encrenaz, T., DeWitt, C., Richter, M., Greathouse, T., Fouchet, T., Montmessin, F., Lefevre, F., Bezard, B., Atreya, S., Aoki, S., Sagawa, H., 2018. New measurements of D/H on Mars using EXES aboard SOFIA. A&A 612, A112. https://doi.org/10.1051/0004-6361/201732367.
Encrenaz, T., DeWitt, C., Richter, M., Greathouse, T., Fouchet, T., Montmessin, F., Lefevre, F., Bezard, B., Atreya, S., Case, M., Ryde, N., 2016. A map of D/H on Mars in the thermal infrared using EXES aboard SOFIA. Astron. & Astophys. 586, A62. https://doi.org/10.1051/0004-6361/201527018.
Eparvier, F., Chamberlin, P., Woods, T., Thiemann, E., 2015. The solar extreme ultraviolet monitor for MAVEN. Space Sci. Rev. 195 (1–4), 293–301. https://doi.org/10.1007/s11214-015-0195-2.
Fedorova, A., Bertaux, J.-L., Betsis, D., Montmessin, F., Korablev, O., Maltagliati, L., Clarke, J., 2017. Water vapor in the middle atmosphere of Mars using the 2007 global dust storm. Icarus 300, 440–457. https://doi.org/10.1016/j.icarus.2017.09.025.
Fedorova, A., Korablev, O., Bertaux, J.-L., Rodin, A., Kiselev, A., Perrier, S., 2006. Mars water vapor abundance from SPICAM IR spectrometer: seasonal and geographic distributions. J. Geophys. Res. 111, E09S08. https://doi.org/10.1029/2006JE002695.
Fedorova, A., et al., 2020. Stormy water on Mars: the distribution and saturation of atmospheric water during the dusty season. Science. https://doi.org/10.1126/science.aay9522.
Feldman, P.D., et al., 2011. Rosetta-Alice observations of exospheric hydrogen and oxygen on Mars. Icarus 214 (2), 394–399.
Forbes, J.M., Lemoine, F.G., Bruinsma, S.L., Smith, M.D., Zhang, X., 2008. Solar flux variability of Mars' exosphere densities and temperatures. Geophys. Res. Lett. 35, L01201. https://doi.org/10.1029/2007GL031904.
Galli, A., Wurz, P., Lammer, H., Lichtenegger, H.I.M., Lundin, R., Barabash, S., Grigoriev, A., Holmstr, M., Gunell, H., 2006. The hydrogen exospheric density profile measured with ASPERA-3/NPD. Sp. Sc. Rev. 126 (1–4), 447–467.
Halekas, J.S., 2017. Seasonal variability of the hydrogen exosphere of Mars. J. Geophys. Res. Planets 122, 901–911. https://doi.org/10.1002/2017JE005306.
Heavens, N.G., et al., 2018. Hydrogen escape from Mars enhanced by deep convection in dust storms. Nature Astronomy 2, 126–132.
Hendrix, A., et al., 2020. Ultraviolet-Based Science in the Solar System: Advances and Next Steps: A white paper submitted to the Planetary Science and Astrobiology Decadal Survey 2023–2032. arXiv 14993v1.
Hunten, D., 1982. Thermal and non-thermal escape mechanisms for terrestrial bodies. Planet. Space Sci. 30, 773–783. https://doi.org/10.1016/0032-0633(82)90110-6.
Jain, S., Soto, E., Evans, J., Deighan, J., Schneider, N., Bougher, S., 2021. Thermal structure of Mars' middle and upper atmospheres: understanding the impacts of dynamics and solar forcing. Icarus. https://doi.org/10.1016/j.icarus.2021.114703.
Jakosky, B., 2021. Atmospheric loss to space and the history of water on Mars. Annu. Rev. Earth Planet. Sci. 49, 71–93. https://doi.org/10.1146/annurev-earth-062420-052845.
Jakosky, B.M., Slipski, M., Benna, P., Mahaffy, M., Elrod, R., Yelle, S. Stone, Alsaeed, N., 2017. Mars' atmospheric history derived from upper-atmosphere measurements of $^{38}Ar/^{36}Ar$. Science 355, 1408–1410. https://doi.org/10.1126/science.aai7721.
Kass, D.M., Kleinböhl, A., McCleese, D.J., Schofield, J.T., Smith, M.D., 2016. Interannual similarity in the Martian atmosphere during the dust storm season. Geophys. Res. Lett. 43, 6111–6118.
Kass, D.M., Schofield, J.T., Kleinbohl, A., McCleese, D.J., Heavens, N.G., Shirley, J.H., Steele, L.J., 2019. Mars Climate Sounder observation of Mars' 2018 global dust event. Geophys. Res. Lett. 46 https://doi.org/10.1029/2019GL083931.
Kleinböhl, A., et al., 2020. Diurnal variations of dust during the 2018 global dust storm observed by the Mars climate Sounder. J. Geophys. Res. 125, e06115.
Krasnopolsky, 2002. Mars' upper atmosphere and ionosphere at low, medium, and high solar activities: Implications for evolution of water. J. Geophys. Res. 107 (E12), 5128. https://doi.org/10.1029/2001JE001809.
Lee, C.O., Jakosky, B.M., Luhmann, J.G., Brain, D.A., Mays, M.L., Hassler, D.M., et al., 2018. Observations and impacts of the 10 September 2017 solar events at Mars: an overview and synthesis of the initial results. Geophys. Res. Lett. 45, 8871–8885. https://doi.org/10.1029/2018GL079162.
Mahaffy, P.R., Benna, M., Elrod, M., Yelle, R.V., Bougher, S.W., Stone, S.W., Jakosky, B. M., 2015. Structure and composition of the neutral upper atmosphere of Mars from the MAVEN NGIMS investigation. Geophys. Res. Lett. 42, 8951–8957. https://doi.org/10.1002/2015GL065329.
Masunaga, K., Yoshioka, K., Chaffin, M., Deighan, J., Jain, S., Schneider, N., Kimura, T., Tsuchiya, F., Murakami, G., Yamazaki, A., Terada, N., Yoshikawa, I., 2020. Martian oxygen and hydrogen upper atmospheres responding to solar and dust storm drivers: Hisaki space telescope observations. J. Geophys. Res. https://doi.org/10.1029/2020JE006500.
Matta, M., Withers, P., Mendillo, M., 2013. The composition of Mars' topside ionosphere: Effects of hydrogen. J. Geophys. Res. Space Physics 118, 2681–2693. https://doi.org/10.1002/jgra.50104.
Mayyasi, M., et al., 2017a. IUVS echelle-mode observations of interplanetary hydrogen: standard for calibration and reference for cavity variations between earth and Mars during MAVEN cruise. J. Geophys. Res. Space Physics 122. https://doi.org/10.1002/2016JA023466.
Mayyasi, M., Clarke, J., Bhattacharyya, D., Deighan, J., Jain, S., Chaffin, M., et al., 2017b. The variability of atmospheric deuterium brightness at Mars: evidence for seasonal depen- dence. J. Geophys. Res. Space Physics 122. https://doi.org/10.1002/2017JA024666.
Mayyasi, M., Bhattacharyya, D., Clarke, J., Catalano, A., Benna, M., Mahaffy, P., et al., 2018a. Significant space weather impact on the escape of hydrogen from Mars. Geophys. Res. Lett. 45, 8844–8852. https://doi.org/10.1029/2018GL077727.
Mayyasi, M., Withers, P., Fallows, K., 2018b. A sporadic topside layer in the ionosphere of Mars from analysis of MGS radio occultation data. J. Geophys. Res. Space Physics 123, 883–900. https://doi.org/10.1002/2017JA024938.
Mayyasi, M., Clarke, J., Bhattacharyya, D., Chaufray, J.Y., Benna, M., Mahaffy, P., et al., 2019a. Seasonal variability of deuterium in the upper atmosphere of Mars. J. Geophys. Res. 124, 2152–2164. https://doi.org/10.1029/2018JA026244.
Mayyasi, M., Narvaez, C., Benna, M., Elrod, M., Mahaffy, P., 2019b. Ion-neutral coupling in the upper atmosphere of Mars: a dominant driver of topside ionospheric structure. J. Geophys. Res. 124 https://doi.org/10.1029/2019JA026481.
McClintock, W., Schneider, N., Holsclaw, G.M., Clarke, J., Hoskins, A., Stewart, I., Montmessin, F., Yelle, R., Deighan, J., 2014. The imaging ultraviolet spectrograph (IUVS) for the MAVEN Mission. Space Sci. Rev. https://doi.org/10.1007/s11214-014-0098-7.
McElroy, M., Donahue, T., 1972. Stability of the Martian Atmospehere. Science 177 (4053), 986–988.
Montmessin, F., Fouchet, T., Forget, F., 2005. Modeling the annual cycle of HDO in the Martian atmosphere. J. Geophys. Res. 110, E03006. https://doi.org/10.1029/2004JE002357.
Montmessin, F., Smith, M., Langevin, Y., Mellon, M., Fedorova, A., 2017. The water cycle. In: Haberle, R., Clancy, R., Forget, F., Smith, M., Zurek, R. (Eds.), The Atmosphere and Climate of Mars (Cambridge Planetary Science). Cambridge University Press, Cambridge, pp. 338–373. https://doi.org/10.1017/9781139060172.011.
Neary, L., et al., 2020. Explanation for the increase in high-altitude water on Mars observed by NOMAD during the 2018 global dust storm. Geophys. Res. Lett. 47, e84354.
Novak, R.E., Mumma, M.J., Villanueva, G.L., 2011. Measurement of the isotopic signatures of water on Mars: Implications for studying methane. Planetary and Space Science 59, 163–168. https://doi.org/10.1016/j.pss.2010.06.017.
Orosei, R., et al., 2018. Radar evidence of subglacial liquid water on Mars. Science. https://doi.org/10.1126/science.aar7268.
Patel, M.R., Sellers, G., Mason, J.P., Holmes, J.A., Brown, M.A.J., Lewis, S.R., et al., 2021. ExoMars TGO/NOMAD-UVIS vertical profiles of ozone: 1. Seasonal variation and comparison to water. J. Geophysical Research: Planets 126. https://doi.org/10.1029/2021JE006837 e2021JE006837.
Qin, J., 2021. Solar cycle, seasonal, and dust-storm-driven variations of the mars upper atmospheric state and H escape rate derived from the Lyα emission observed by NASA's MAVEN mission. Astrophys. J. 912, 77. https://doi.org/10.3847/1538-4357/abed4f.
Sanchez-Lavega, A., 2015. An Introduction to Planetary Atmospheres, ISBN 13: 9781420067323. Blackwell's, Oxford, OX, United Kingdom.

Scheller, E., Ehlmann, B., Hu, R., Adams, D., Yung, Y., 2021. Long-term drying of Mars by sequestration of ocean-scale volumes of water in the crust. Science. https://doi.org/10.1126/science.abc7717.

Shaposhnikov, D.S., Medvedev, A.S., Rodin, A.V.V., Hartogh, P., 2019. Seasonal water "pump" in thermosphere of Mars: vertical transport to the thermosphere. GeophysicalResearch Letters 46, 4161–4169. https://doi.org/10.1029/2019GL082839.

Shaposhnikov, D.S., Medvedev, A.S., Rodin, A.V., Yiğit, E., Hartogh, P., 2022. Martian dust storms and gravity waves: disentangling water transport to the upper atmosphere. Journal of Geophysical Research: Planets 127. https://doi.org/10.1029/2021JE007102 e2021JE007102.

Stone, S.W., Yelle, R.V., Benna, M., Elrod, M.K., Mahaffy, P.R., 2018. Thermal structure of the Martian upper atmosphere from MAVEN NGIMS. J. Geophys. Res. Planets 123, 2842–2867. https://doi.org/10.1029/2018JE005559.

Stone, S., Yelle, R., Benna, M., Lo, D., Elrod, M., Mahaffy, P., 2020. Hydrogen escape from Mars is driven by seasonal and dust storm transport of water. Science 370, 824–831. https://doi.org/10.1126/science.aba5229.

Thiemann, E.M.B., Chamberlin, P.C., Eparvier, F.G., Templeman, B., Woods, T.N., Bougher, S.W., Jakosky, B.M., 2017. The MAVEN EUVM model of solar spectral irradiance variability at Mars: algorithms and results. Journal of Geophysical Research: Planets 122, 2748–2767. https://doi.org/10.1002/2016JA023512.

Vandaele, et al., 2019. Martian dust storm impact on the atmospheric H_2O and D/H observed by ExoMars Trace Gas Orbiter. Nature 568, 521–525. https://doi.org/10.1038/s41586-019-1097-3.

Villanueva, G.L., Mumma, M., Novak, R., Käufl, H., Hartough, P., Encrenaz, T., Tokunaga, A., Khayat, A., Smith, M., 2015. Strong water isotopic anomalies in the martian atmosphere: probing current and ancient reservoirs. Science Reports 348, 6231. https://doi.org/10.1126/science.aaa3630.

Villanueva, G.L., et al., 2021. Water heavily fractionated as it ascends on Mars as revealed by ExoMars/NOMAD. Sci. Adv. 7 https://doi.org/10.1126/sciadv.abc8843.

Villanueva, G.L., Liuzzi, G., Aoki, S., Stone, S., Brined, A., Thomas, I., Lopez-Valverde, M., Trompet, L., Erwin, J., Daerden, F., Ristic, B., Smith, M., Mumma, M., Faggi, S., Kofman, V., Robert, S., Neary, L., Patel, M., Bellucci, G., Lopez-Moreno, J., Vandaele, A.-C., 2022. The Deuterium Isotopic Ratio of Water Released from the Martian Caps as Measured with TGO/NOMAD, submitted to GRL (under review).

Yung, Y., Wen, J.-S., Pinto, J., Allen, M., Pierce, K., Paulson, S., 1988. HDO in the Martian atmosphere: implications for the abundance of crustal water. Icarus 76, 146–159 (0019-1035/88).

Zurek, R., Chicarro, A., Allen, M.A., et al., 2011. Assessment of a 2016 mission concept: the search for trace gases in the atmosphere of Mars. Planet. Space Sci. 59, 284–291.

Zurek, R., Martin, L., 1993. Interannual Variability of Planet-Encircling Dust Storms on Mars. J. Geophys. Res. 98 (E2), 3247–3259, 92JE02936.